J. Fluid Mech. (1990), *vol.* 211, *pp.* 463–495
Printed in Great Britain

The influence of wave breaking on the surface pressure distribution in wind–wave interactions

By MICHAEL L. BANNER

School of Mathematics, University of New South Wales, PO Box 1, Kensington, NSW 2033, Australia

(Received 19 March 1986 and in revised form 8 August 1989)

In reviewing the current status of our understanding of the mechanisms underlying wind-wave generation, it is apparent that existing theories and models are not applicable to situations where the sea surface is disturbed by breaking waves, and that the available experimental data on this question are sparse. In this context, this paper presents the results of a detailed study of the effects of wave breaking on the aerodynamic surface pressure distribution and consequent wave-coherent momentum flux, as well as its influence on the total wind stress.

Two complementary experimental configurations were used to focus on the details and consequences of the pressure distribution over breaking waves under wind forcing. The first utilized a stationary breaking wave configuration and confirmed the presence of significant phase shifting, due to air flow separation effects, between the surface pressure and surface elevation (and slope) distributions over a range of wind speeds. The second configuration examined the pressure distribution, recorded at a fixed height above the mean water surface just above the crest level, over short mechanically triggered waves which were induced to break almost continuously under wind forcing. This allowed a very detailed comparison of the form drag for actively breaking waves and for waves of comparable steepness just prior to breaking ('incipiently' breaking waves). For these propagating steep-wave experiments, the pressure phase shifts and distributions closely paralleled the stationary configuration findings. Moreover, a large increase (typically 100%) in the total windstress was observed for the breaking waves, with the increase corresponding closely to the comparably enhanced form drag associated with the actively breaking waves.

In addition to further elucidating some fundamental features of wind-wave interactions for very steep wind waves, this paper provides a useful data set for future model calculations of wind flow over breaking waves. The results also provide the basis for a parameterization of the wind input source function applicable for a wave field undergoing active breaking, an important result for numerical modelling of short wind waves.

1. Introduction

Over the last three decades, an elucidation of the basic mechanisms involved in the wind generation of water waves has been the subject of intensive theoretical and experimental investigation, typically involving analysis or measurements of either monochromatic waves or of a spectrum of wave components. While the spectral approach is more appropriate for naturally occurring wind waves, the former approach offers considerable simplification in the analysis and experiments. Recent

developments in wind-wave dynamics, subsequent to the comprehensive review article of Barnett & Kenyon (1976), have led to further improvements in our current understanding of the dynamics of wind waves. Interest in this problem has been heightened in recent years by the fundamental role of very short surface-wave components in active microwave remote sensing of the oceans, using techniques based on Bragg backscattering, such as in the scatterometer determination of ocean wind stress and in ocean wave imaging by synthetic aperture radar techniques. The local spectral density of the water-surface wavenumber component which is in Bragg resonance with the incident microwave wavenumber vector is believed to determine the local microwave backscatter level (Plant & Wright 1977). Depending on the particular sensor arrangement, these techniques have been shown to offer the potential capability for monitoring the dominant ocean directional wave spectrum, the ocean windstress, internal waves, fronts, currents and shallow-water bathymetry under a wide range of ambient conditions. A proper understanding of the dynamics underlying the evolution of short-wave spectra is of central importance in improving our presently incomplete knowledge of the transfer functions of these microwave devices.

A suitable mathematical description for the evolution of the short wavenumber components of the wind-wave spectrum is provided by the radiative transfer equation (see Phillips 1977, §12). According to this formulation, the evolution of the energy or action density of a spectral component is the resultant of the direct wind input, nonlinear spectral transfer to and from this component and dissipation due to breaking and viscous effects. For very short fetches situations appropriate to wind-wave tanks, recent laboratory studies (e.g. Plant & Wright 1977; Wu, Hsu & Street 1977; Plant 1980) have contributed significant insight into these terms, with most investigations having been concerned with determining the wind input source function. In this context, the work of Plant & Wright (1977) has demonstrated the strong influence of nonlinear spectral transfers for wave components longer than about 0.10 m and hence the necessity to take these effects into account when interpreting observed spectral wind-wave growth rates.

A conspicuous feature of water waves evolving under wind forcing is wave breaking, which manifests in the familiar form of whitecaps for wavelengths in excess of around 0.3 m, and in the less obvious but more ubiquitous form of microscale breaking of the shorter wavelength components, which proceeds without significant air entrainment. In the open ocean, breaking occurs from a variety of contributing mechanisms, including excessive hydrodynamical straining by longer wave components, local reinforcement by focusing of neighbouring directional wave components as well as aerodynamic forcing. The relative importance of the local wind forcing in influencing the geometry and evolution of breaking waves is largely unknown. What has been established is that local air flow separation occurs concomitantly with wave breaking (Banner & Melville 1976; Kawai 1981, 1982), with a potentially significant augmentation of the local windstress (Banner & Melville 1976), wave-coherent momentum flux due to the pressure forces (form drag) (Banner 1986) and to tangential stresses (Okuda, Kawai & Toba 1977). Laboratory observations suggest that wave components with u_*/c sufficiently large (i.e. $O(1)$) will be involved in breaking, at least intermittently. Here u_* is the wind friction velocity and c is the phase speed of the wave components. These observations are consistent with the addition of significant levels ($O(0.25)$) of wave momentum each wave period (as will be discussed later in this paper) for which the onset of breaking is hardly

surprising. This broad classification in terms of u_*/c hardly addresses other basic questions concerning the role of the windstress in influencing the geometrical and evolutionary properties of breaking wind waves and consequent questions such as whether the duration of breaking events is sufficient for their effects to be incorporated locally in the air flow and the extent to which their effects are aerodynamically significant in wind-wave interactions. Although our current knowledge does not provide comprehensive answers to such fundamental questions, certain results of recent investigations provide useful insight, as summarized below.

Previous laboratory studies of the character of the air flow over propagating wind waves (e.g. Kawai 1981, 1982; Chang, Plate & Hidy 1971) have documented the occurrence of air flow separation thereby confirming the ability of the air flow to respond to the breaking configuration despite its intermittency: the present study adds further confirmation.

On the question of the wind influence on the shape of breaking waves, the available data is generally confused by contributions from non-breaking waves. The most detailed study of this aspect for short wind waves appears to be the study by Koga (1984), who examined the geometrical characteristics of a large ensemble of wind waves, predominantly at a single very high windstress ($u_* = 1.48$ m/s) with some auxiliary lower friction velocity data for $u_* = 0.56$ m/s. Koga used a classification of breaking/non-breaking waves based on air entrainment and it is not straightforward to relate this classification method to situations involving active micro-scale breaking, as in the present study. Koga found that at the higher windstress levels, the wave forms tended to be more sharp-crested. However, in the same context, it is interesting to note that based on their radar backscatter measurements, over a comparably large friction velocity range, Plant & Wright (1977) did not observe any significant change with increasing u_* in the r.m.s. amplitude of given wavenumber spectral components once they had saturated, suggesting that the windstress has no significant net effect on the gross geometry of the wavenumber components investigated.

A detailed laboratory investigation of the near-surface wind pressure field over an evolving wind wave spectrum at short fetches was reported by Wu *et al.* (1977), as part of an experiment aimed at examining the evolution of the wave spectrum via the transport equation. Their measurements included the cross-spectrum between the near-surface fluctuating pressure (at a fixed height above the mean water level just above the crest level) and the instantaneous water-surface elevation. The wind waves at the spectral peak under the strong forcing conditions of their study were necessarily breaking, at least intermittently and the reported phase shifts of 40°–45° between the pressure and surface elevation for the spectral peak Fourier component implies significant levels of form drag. However, the physical mechanisms associated with these phase shifts were not investigated. In the similar context of strongly forced wind waves, Okuda *et al.* (1977) have proposed that a strong intermittent tangential stress mechanism is operative, based on their observations of the distribution of the local mean velocity gradient in the water surface layer for very short (4 Hz) saturating gravity wind waves in the laboratory. This is consistent with the shear stress rise at the point of reattachment of separated flow over solid waves (e.g. see Buckles, Hanratty & Adrian 1984). Working at a very short fetch (2.85 m) and under very strong forcing conditions ($u_*/c \gtrsim 1$), Okuda *et al.* (1977) reported large shear stress concentrations along the windward side of the wave profile, peaking at the crest, with vanishingly small levels of shear stress in the water on the

leeward side. The resulting associated mean shear stress $\bar{\tau}$ and wave-coherent surface shear stress in the water τ_s^w are conveniently estimated by

$$\bar{\tau} = \langle \tau_s \rangle, \quad \tau_s^w = \langle \tau_s u_s \rangle / c,$$

where τ_s, u_s are the distributions of surface shear stress and surface velocity respectively and $\langle\ \rangle$ denotes a phase average. From the shear stress distributions reported by Okuda *et al.*, these instantaneous levels of $\bar{\tau}$ were in excess of the total wind stress determined over the ensemble of all waves passing their measurement site. On this basis, they concluded that this skin friction mechanism was dominant, with the normal stresses of secondary importance as regards transfers to wind waves saturating under strong wind forcing. However, the unknown intermittency factor associated with the duration of saturating wave components and with the associated shear stress spikes makes it difficult to assess accurately their overall contribution to the mean stress: furthermore their wave-coherent contribution τ_s^w is arguably smaller (see Banner 1986). Their conclusions on the relative dominance of the wave-coherent contributions of shear stress for breaking wind waves are reviewed in relation to the findings of the present study in §5. Okuda (1981, 1982*a*, *b*) extended the study of Okuda *et al.* (1977), exploring the vorticity, streamline and pressure distributions below very short wind waves as inferred from subsurface hydrogen bubble and micro-bead measurements. In this context, it should be noted that the quoted uncertainty in the pressure determinations (± 2 Pa) in Okuda (1982*b*) precludes the use of this method in assessing the surface pressure distribution induced by the wind, which has a comparable magnitude according to the results of present study. Based on the findings of Okuda *et al.* (1977) and Okuda (1982*a*), Csanady (1985) proposed a model for air–sea momentum transfer based on the aerodynamic and hydrodynamic consequences of the locally separating and reattaching air flow over saturating short-crested wavelets. The implications of this model for field observations were also considered.

On the closely related question of spectral wind-wave growth rates, Plant (1982) has correlated the available experimental data on wind-wave growth over a wide range of wind and wave conditions, based on single wave and spectral component experiments. As a result, he proposed the following form of the wind input source function $S_{in}(\boldsymbol{k})$ for the evolution of the wavenumber spectrum $\psi(\boldsymbol{k}; \boldsymbol{x}, t)$

$$S_{in}(\boldsymbol{k}) = 0.04(\pm 0.02)\frac{u_*^2}{c}|\boldsymbol{k}| \cos\theta\, \psi(\boldsymbol{k}), \tag{1.1}$$

where u_* is the wind friction velocity, c is the phase speed of the wavenumber component $\boldsymbol{k}$ and θ, $(-\frac{1}{2}\pi \leqslant \theta \leqslant \frac{1}{2}\pi)$ is the angle between the wind and wave directions, applicable for the range $u_*/c \gtrsim 0.1$. Clearly (1.1) may need to be modified for opposing winds and in the presence of local underlying larger-scale currents. Mitsuyasu & Honda (1982) studied the growth rates of single-component mechanical waves, varying the surface roughness by adding surfactant and found a similar result to (1.1). Al-Zanaidi & Hui (1984) proposed a variant of (1.1) using U_λ, the windspeed at a height of one wavelength, instead of u_*. However, according to Mitsuyasu & Kusaba (1988), this produces no systematic improvement in the accuracy of the parameterization of the input source function. For weaker wind forcing conditions i.e. $u_*/c \lesssim 0.1$, the detailed field measurements of Snyder *et al.* (1981) indicate that $S_{in}(\boldsymbol{k})$ transitions to a different dependence on u_*/c.

Theoretical models have also been used to determine parameterizations of the wind input source function. The numerical models of Gent & Taylor (1976), Gent

(1977), Taylor *et al.* (1977) and Al-Zanaidi & Hui (1984) explored in detail how the input source function varied as a function of various parameters, particularly the wind-to-wave speed ratio and the distribution of surface roughness, showing the relative contributions of the normal and tangential stresses, with the normal component providing the dominant contribution by a wide margin. These models used various closure schemes and different treatments of the surface-layer air flow. Gent & Taylor (1976) and Gent (1977) assumed fully rough turbulent air flow and explored the effect of different roughness length distributions along the wave surface. Al-Zanaidi & Hui (1984) considered aerodynamically smooth, transitional and fully rough air-flow regimes, calculating the viscous sublayer flow as part of the solution. Both models demonstrated the importance of surface roughness in the interfacial coupling process. Gent & Taylor (1976), Gent (1977) and Taylor *et al.* (1977) also explored the effect of a moderate waveform steepness on the input source function, reporting that increasing the wave slope did not result in a proportional increase in the input to the wave field. More closely allied to the present investigation are the papers by Gent & Taylor (1977) and Taylor *et al.* (1977) in which the effects of very large wave profile steepness were investigated. The relevant results of their papers are considered in detail in §5 below.

The present contribution is aimed at exploring in detail the effect of wave breaking on the pressure distribution of the wind on the wavy water surface and hence on the wave-coherent pressure-waveslope momentum flux (i.e. form drag) from the wind to the wave field, and its contribution to the overall windstress. Two complementary experimental configurations have been used in this investigation. In common with the previous studies of Banner & Melville (1976) and Banner (1986), the first phase of the experiment utilized a quasi-steady, spatially stationary breaking wave, induced by a fixed subsurface hydrofoil in a water tunnel, as described in detail in §2. The motivation for this configuration was to circumvent the well-documented difficulties inherent in measuring aerodynamic surface pressure over propagating water waves (e.g. Papadimitrakis 1982; Young 1983), here complicated by the additional effects of the unsteadiness and air flow separation associated with the breaking events. The complementary second phase examined and extended the applicability of the quasi-steady configuration results to propagating wind-driven waves for both breaking and incipiently breaking waves under strong wind forcing conditions.

It is felt that these complementary experiments provide a set of reliable measurements which is free from most of the difficulties inherent in any alternative assessment, and which illustrates and quantifies the typical aerodynamic surface pressure effects associated with wind blowing over breaking wind waves.

A detailed description of the probing technique and the experimental results is followed by discussion on the implications of these findings for air–sea interaction and for the modelling of the wind input source function for wind-wave fields undergoing active wave breaking.

2. Experimental procedure

The aim of this study was to investigate quantitatively the influence of wave breaking on the wind pressure distribution on the water surface and its implications for the wave-coherent and total momentum fluxes to the sea surface.

Of central importance in the study was the accurate determination of the surface pressure associated with blowing over propagating water waves, a challenging

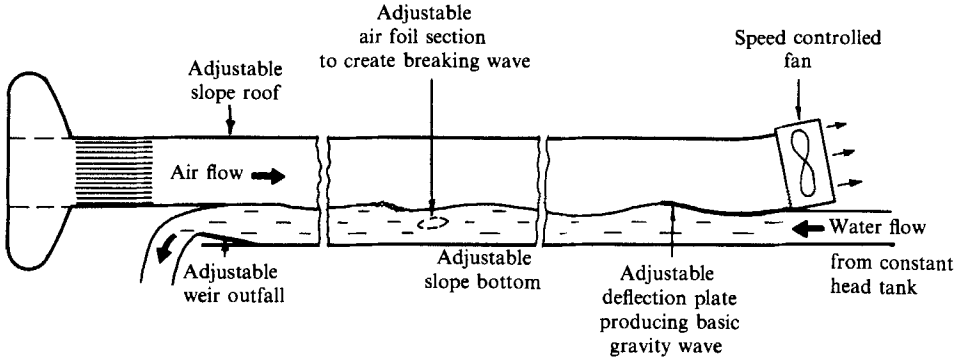

FIGURE 1. Wind-wave flume configuration for stationary breaking-wave experiments: working length 7.3 m; channel width 0.225 m; air channel depth 0.36 m; water channel depth 0.22 m; working section halfway along channel.

experimental task owing to several complicating factors. These include the need to maintain the pressure probe elevation at a small, fixed height above the underlying moving water surface and the avoidance of spurious signals due to motion of the pressure transducer on a wave-following servo system, mechanical vibrations from various sources as well as standing and propagating acoustic waves in the air flow. Most of these problems were circumvented in this study by the use of a combination of two complementary wind-wave tank configurations. Also, as a precursor to the main investigation, a significant effort was devoted to the reliable determination of the static pressure in the highly sheared flow overlying the air–water interface which is subject to the additional effects of air flow separation in the lee of the breaking crests. Of the limited choice of sensors, it was decided that a pressure disk probe was potentially the most suitable. A small contoured disk probe (10 mm diameter, 1.2 mm maximum thickness) was fabricated and tested against a 2.3 mm diameter standard NPL elliptic-nosed Pitot-static tube in the free stream of the wind-wave tank described below. The pressure transducer used for the calibration and subsequent data collection throughout this study was a thermally-stabilized Barocel differential electronic manometer used on a range of ± 4 Pa. Complementary mean velocity profile data was generally determined from Pitot-static tube determinations, with the exception of the total windstress measurements in the second phase of the experiment based on the logarithmic profile method. For this data, a counter-type laser anemometer (which became available later in this study) was used to avoid any influence of the vertically varying streamwise turbulence intensity on Pitot-static tube measurements.

2.1. *Stationary wave configuration*

During the first phase of the study which included the evaluation of the disk pressure probe, the wave tank was set up as a flume in which the flowing stream created a stationary wavetrain containing a quasi-steady spilling breaker. This arrangement is shown in figure 1. An overlying wind flow was provided by a speed-controlled axial flow fan used in the suction mode. The background wavetrain was produced by the deflection plate at the water entry and the breaking wave was created by a suitably inclined subsurface hydrofoil (91 mm length, 22 mm chord thickness) located within the working section at a depth of 120 mm, about midway along the tank. It should be noted that hydrofoil provided the main source for sustaining the breaking wave,

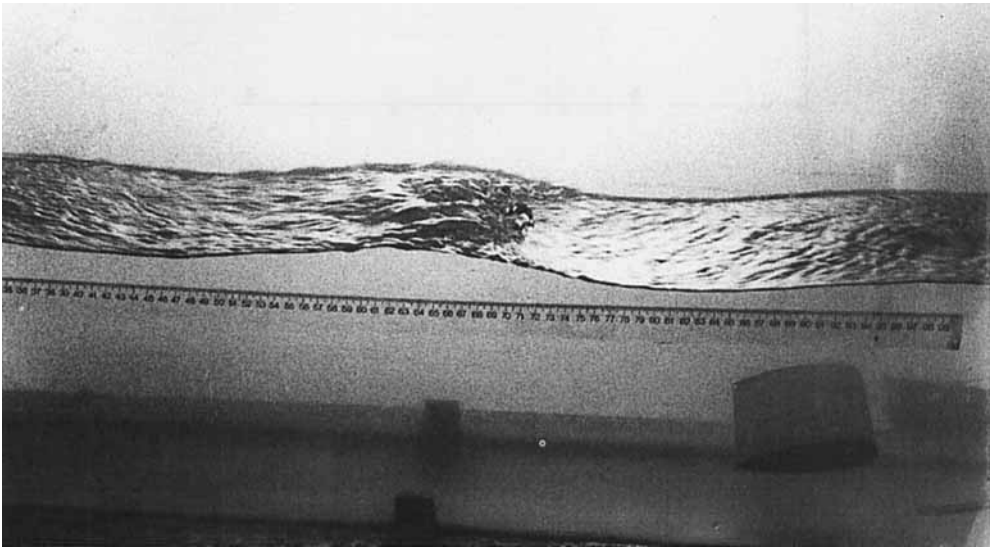

FIGURE 2. Typical stationary breaking wave. The auxiliary lengthscale is in cm. The wind direction is from left to right.

with some secondary influence from the wind field, depending on its strength. This arrangement provided the desired quasi-stationary breaking wave conditions sought in this phase of the study, in which the water speed was maintained at 0.79 m/s, producing a gently spilling breaker with a wavelength of 0.34 m, within a train of unbroken waves with 0.4 m wavelength. A typical stationary breaking wave is shown in figure 2. The roof of the flume was adjusted to provide zero mean pressure gradient along the working section. Lateral Pitot-static tube traverses showed that the mean velocity field was laterally uniform to within about 1 % over the central region of the air channel at each of the centreline wind speeds (U_c = 2.6, 3.8 and 5.4 m/s) used in this phase of the study, which embraced the lowest wind speed for reliable pressure measurements and the highest wind speed before the onset of long-period seiching of the water in the flume. Using the centre-height wind speed U_c as the reference velocity, for intercomparison with the complementary propagating wave study, the equivalent reference wind speed U_∞ over water at rest was taken as $U_\infty = U_c + c$, where c is the phase speed over water at rest. This provided an effective U_∞/c range of 4.3–7.8, corresponding approximately to u_*/c in the range 0.2–0.4, based on the approximate empirical correspondence $u_* \sim 0.05U$ typically found for the friction velocity u_* in wave tanks (e.g. Plant & Wright 1977). Owing to the streamwise inhomogeneity of the flow field associated with the stationary breaking wave, the usual logarithmic mean velocity profiling method was not appropriate, while the poor accuracy of the momentum integral method precluded its use. However, the friction velocity was determined for the complementary propagating wave study described subsequently in §2.2.

This configuration also facilitated an initial detailed intercomparison between the Pitot-static and disk probe performance and subsequently, accurate measurements of the surface pressure distribution over a region of the wavy water surface which included the breaking wave. The results of the calibration in the free stream of the wind channel are shown in figure 3 where the disk pressure p_d, Pitot-static tube

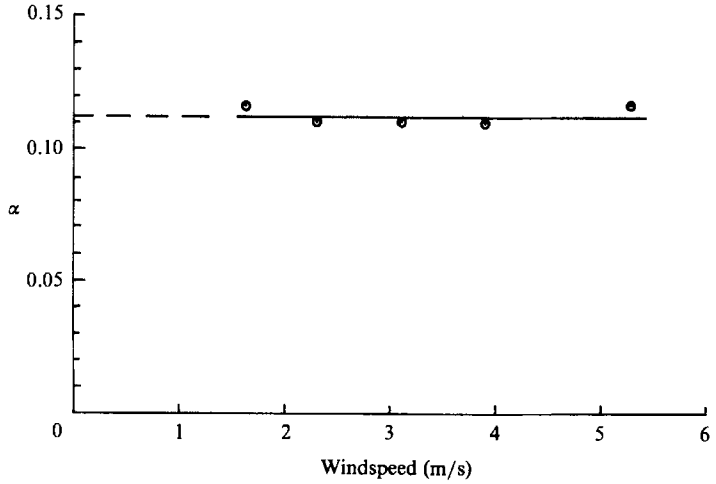

FIGURE 3. Disk probe calibration.

pressure p_s and dynamic free-stream pressure $\frac{1}{2}\rho_a U^2$ were used to form the dimensionless combination $\alpha = (p_s - p_d/\frac{1}{2}\rho_a U^2$ which is shown plotted against U. It is evident that the variation in the disk coefficient α from the value 0.112 was negligible and this value was adopted throughout this study. Evidently, the disk pressure is related to the true static pressure to a good approximation by

$$p_d = p_s - \tfrac{1}{2}\alpha\rho_a U^2, \tag{2.1}$$

and to deduce p_s, the local mean velocity is required. This was obtained by installing a United Sensors Kiel tube (shielded total tube) with an outside diameter of 3.175 mm alongside the disk at a separation of 40 mm, taking care to align the sensing locations. The Kiel tube has a claimed free-stream response

$$p_{\text{Kiel}} = p_s + \tfrac{1}{2}\rho_a U^2, \tag{2.2}$$

applicable over a wide range (up to 45°) of approach flow directions. Calibration against a standard total tube revealed that (2.2) was a good approximation over inclination angles up to about 35° over the velocity range of interest here.

The pressure lines from the combination disk–Kiel probe (hereafter referred to as the combination sensor, shown in figure 4) were connected to a pressure switch so that either the disk pressure or Kiel tube pressure could be fed to one port of the electronic manometer. The other port was referenced to a NPL (Pitot)-static probe held at a fixed location in the free stream downwind from the test section. For the stationary wave measurements the disk and Kiel probes were symmetrically displaced about the air channel centreline. Typically, averaging times of the order of 5 min, using a time constant of 100 s, were required to obtain repeatable readings.

A preliminary test was conducted to evaluate the combination sensor performance in a region of the flow where the Pitot-static tube might be expected to perform reliably. A horizontal traverse was made from the breaking crest to the crest ahead (downwind) of it, at a height of 30 mm above the crest level at a centreline windspeed of 5.3 m/s. Figure 5(*a*) summarizes the details of this traverse, showing the traverse path and the measured static pressures. It is seen that both probing systems indicate similar pressure distributions, with the phases of the maximum and minimum values corresponding closely, but with the combination sensor indicating a 10% greater

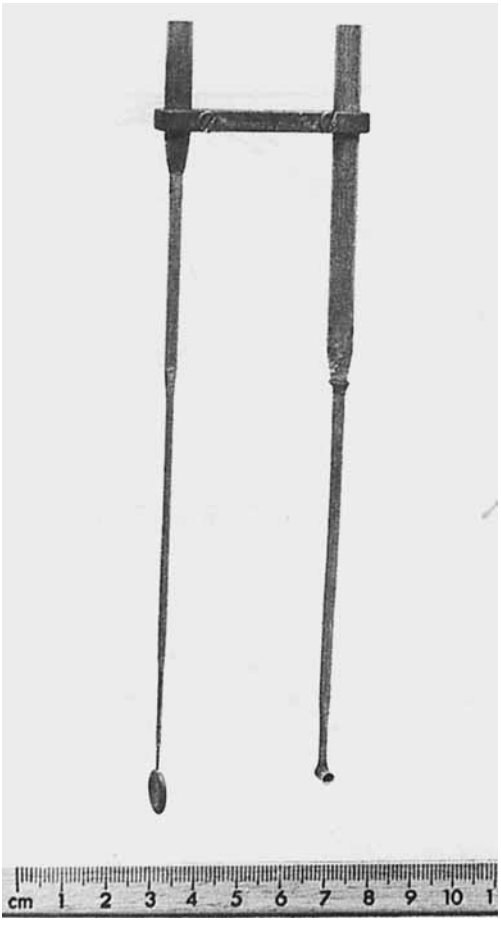

FIGURE 4. Disk (left) and Kiel tube (right) probes used for the pressure determinations in this study.

overall variation. This provides a useful indication of the uncertainty associated with the pressure determinations. Also shown is the variation along the traverse path of the correction term $\frac{1}{2}\alpha\rho_a U^2$, suggesting that previous studies in which a disk alone was used to infer the static pressure would have been subject to this source of error. The effect on the wave-slope-coherent momentum flux would then depend on the phasing between the pressure, the velocity and the surface slope which enter into the momentum flux computation

$$\left\langle p_s \frac{\partial \eta}{\partial x} \right\rangle \sim \langle (p_d + \tfrac{1}{2}\alpha\rho_a U^2)\, \eta_x \rangle. \tag{2.3}$$

From the particular distribution of $\frac{1}{2}\alpha\rho_a U^2$ found here at a fixed height above the mean water level it appears that its neglect is justified, but it should not be assumed negligible *a priori*, especially for wave follower studies over breaking waves where stronger asymmetrics in the near-surface velocity field are to be expected. Closer to the interface, within the separation region, the combination probe registered the same static pressure as the Pitot-static tube, consistent with the negligibly small local velocity there.

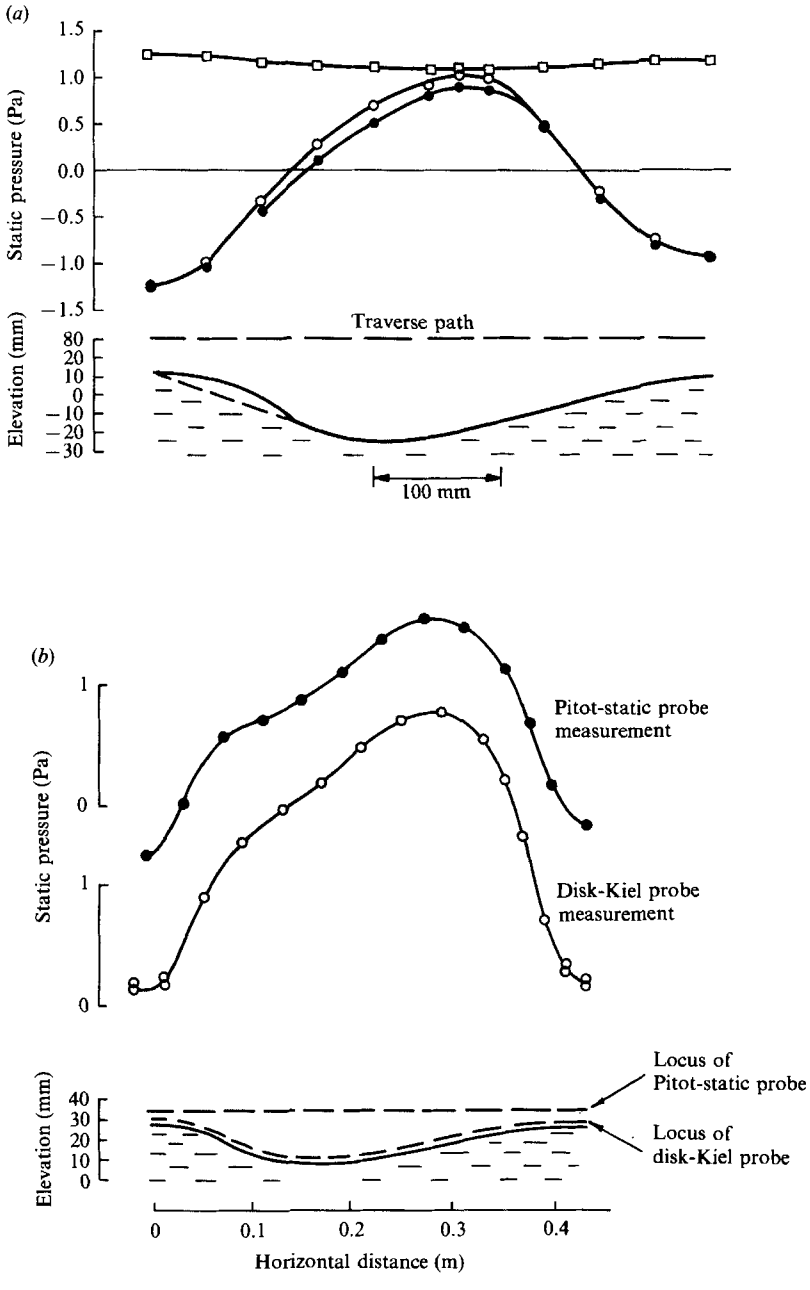

FIGURE 5. Performance comparisons of pressure sensed by ○, disk-Kiel tube probes and by ●, a standard NPL 2.3 mm dia. Pitot-static tube along traverse paths indicated over stationary breaking waves. (*a*) Pressure and velocity correction term (□) at a fixed height above the mean water level. The centreline windspeed was 5.3 m/s from left to right. (*b*) Difference between fixed height and surface-following pressure determination. The centreline wind speed was 4 m/s from left to right (after Banner 1986).

It should also be noted that in figure 4 of the preliminary study reported by Banner (1986) (reproduced here in figure 5*b*) a similar technique was used to establish that the pressure distribution over a breaking wave determined by a horizontal traverse just above the crest level closely paralleled the pressure sensed by traversing along the actual surface, with the surface pressure variation over a breaking wavelength attenuated by a factor of about 0.85–0.9 from its surface value.

The combination probe was then used to determine the local surface pressure over the wavy water surface, from the upwind trough with respect to the breaking crest to just beyond the crest of the unbroken wave ahead of the breaking wave. Complementary measurements of the water-surface elevation were made with a traversing wave height gauge whose calibration was linear. The voltage output from the wave gauge was fed to the averaging digital voltmeter to obtain the local mean water elevation. The registration between the pressure sensor location and surface profile location was monitored very carefully using a theodolite sighting system.

Generally, the surface pressure was determined by extrapolating three near-surface determinations at different heights above the local water surface. In addition, more extensive vertical profiling was carried out at a limited number of selected sites. Using the calibration parameters for the pressure sensors and the wave gauge together with the sensor registration data, computer processing of the pressure and water surface elevation (voltage) values for the three wind speeds generated distributions of local pressure, velocity and surface elevation. These files were used to provide graphical output and for further analysis as described in §3.1.

In summary, the preliminary evaluation of the pressure disk sensing system provided a large measure of confidence for its use in this investigation, for both the stationary wave measurements and the complementary propagating wind-wave determinations which are described below.

2.2. *Propagating-wave configuration*

The second phase of the investigation was undertaken to examine the applicability of the stationary breaking-wave findings to the case of propagating wind-forced waves which were induced to break almost continuously in the working section through wind action. This was motivated in part by the possible sensitivity of the stationary breaking-wave findings to their particular geometry and also the possible reduction in their net impact in the context of propagating wind waves because of the intermittency of the breaking. For this configuration both the wave-coherent momentum flux due to pressure forcing and the total wind stress were determined. To highlight the significance of the breaking, parallel measurements were carried out for waves of comparable steepness just prior to breaking ('incipiently breaking') under similar wind conditions.

For this phase, the flume was converted to a propagating wind-wave tank as shown in figure 6, with the working section centred at a fetch of 2.5 m from the air-flow inlet. A novel feature of the air flow was the use of an open roof section 650 mm in length spanning the working section. The motivation for its use is described in detail subsequently. A wave paddle provided an initial monochromatic train of waves with a prescribed frequency. The initial wave slope was set at the wave paddle so that the two desired wind-wave conditions, almost continuously breaking and incipiently breaking, were realized in the working section under the action of the wind, set at a free-stream level of 5.5 m/s throughout these experiments. This required initial wave slopes approximately 0.2 and 0.15 respectively. Two different dominant water wavelengths were investigated: ~ 0.14 m and ~ 0.21 m, corre-

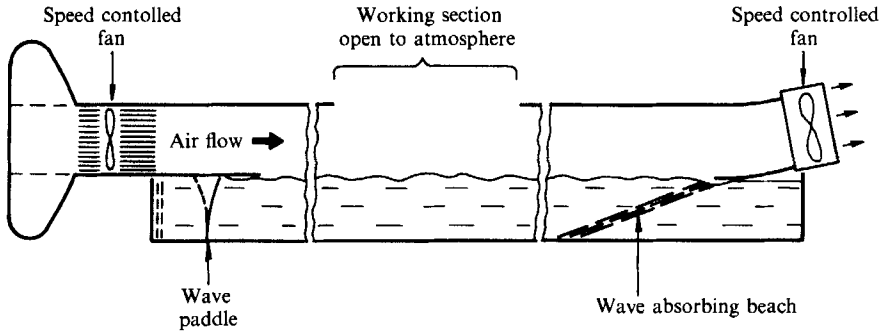

FIGURE 6. Wind-wave flume configuration for propagating wave experiments. Working section open to atmosphere was 0.65 m in length, centred 2.5 m from upwind air flow exit plane. Other dimensions as in figure 1.

sponding to dominant frequencies of 3.35 Hz and 2.85 Hz respectively. In this study, the percentage of breaking waves passing through the measurement site is a fundamental parameter. It was assessed using a detection scheme based on the slope discontinuity at the toe of the spilling region of breaking wind waves, as suggested originally by Longuet-Higgins & Smith (1983) in a field application and investigated in further detail in a laboratory study by Xu, Hwang & Wu (1986). Here, the wave elevation was sampled at 200 Hz in 60 s bursts and the statistics of the slope exceedance were calculated. This was repeated several times to increase the statistical reliability. It was found that this method provided a reliable discrimination between the incipient breaking and spilling breaking waves investigated in this study. Further details of the detection scheme are described in §3.2 below.

The wave-induced surface pressure was sensed by the pressure disk system just above the crest level, as justified by the preliminary studies discussed above. During this second phase, a revised data collection system was used in which the data was logged via an analog-to-digital converter into a microcomputer for real-time cross-spectral analysis processing as described more fully in §3.2 below. This system recorded the data in bursts, with a local sample rate of 4 kHz, and a rate between bursts of 32 Hz.

Prior to the data collection the frequency response of the amplitude and phase characteristics of the pressure disk probe and associated pressure line were determined very carefully in an airtight calibration chamber over the frequency range of interest. A signal proportional to the applied pressure signal was provided by an electro-optical position-sensing photodiode system attached to the driving piston. First the barocel unit was calibrated and then the complete disk probe/pressure line/barocel system. These characteristics are shown in figure 7. Similar calibrations were done for the Kiel total tube system, and are also shown in figure 7.

A sensing system for the simultaneous determination of the local upwind/downwind wave slope was installed immediately adjacent to the site of the pressure measurements. It consisted of two impedance height gauge wire probes with matched frequency response characteristics, held at a typical fixed streamwise separation in the range 8–9 mm. The wave gauges were checked for possible spurious proximity effects but no detectable interactions were observed. The gauges were calibrated statically and found to have linear voltage-displacement characteristics. Their dynamic response characteristics were determined *in situ* against the local

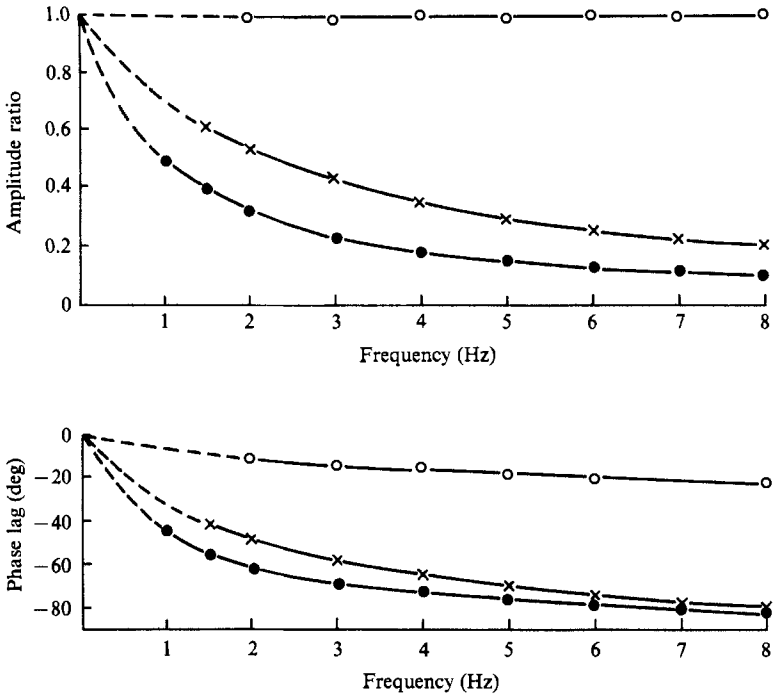

FIGURE 7. Frequency response characteristics for ●, the disk probe, ×, Kiel tube probe and ○, wave height gauges. Upper curve is the amplitude ratio, lower curve is the phase lag in degrees of the sensed signal with respect to the applied signal.

surface elevation signal monitored electro-optically for monochromatic water waves of different frequencies. For these determinations, an 8 mW laser was used with its beam incident tranversely on the air–water interface at near-grazing incidence. The vertical excursions of the reflected beam on the face of a position-sensitive photodiode provided the reference wave amplitude signal with negligible phase lag and amplitude distortion. Over the range of frequencies f (Hz) pertinent to this study, the phase lag in degrees of the height gauges, shown in figure 7, was approximated closely by $8.33f^{\frac{1}{2}}$, with negligible amplitude attenuation. Finally, the ability to record accurately the slope was confirmed dynamically before and after each data run by verifying the match between the measured and computed slope amplitude corresponding to a sinusoidal wavetrain whose waveheight and frequency were recorded by either of the individual height gauges. In addition, the phase of the slope was checked against the phase of the average of the two height gauges, with any deviation from 90° being corrected iteratively through minor adjustments to the height gauge calibration constants. Representative breaking and incipiently breaking propagating waves are shown in figure 8 which also shows the *in situ* pressure disk and slope sensing devices.

During an early determination of the vertical decay of the wave-induced pressure field, it was noticed that the decay was initially quasi-exponential, but instead of decaying to zero, the wave-induced pressure persisted in the free stream and above at a constant level of about 0.1 of the near-surface level. Noting the possibility of spurious results as might arise owing to finite duct cross-section influence on the free-stream velocity and hence pressure, as well as standing wave modes, preliminary

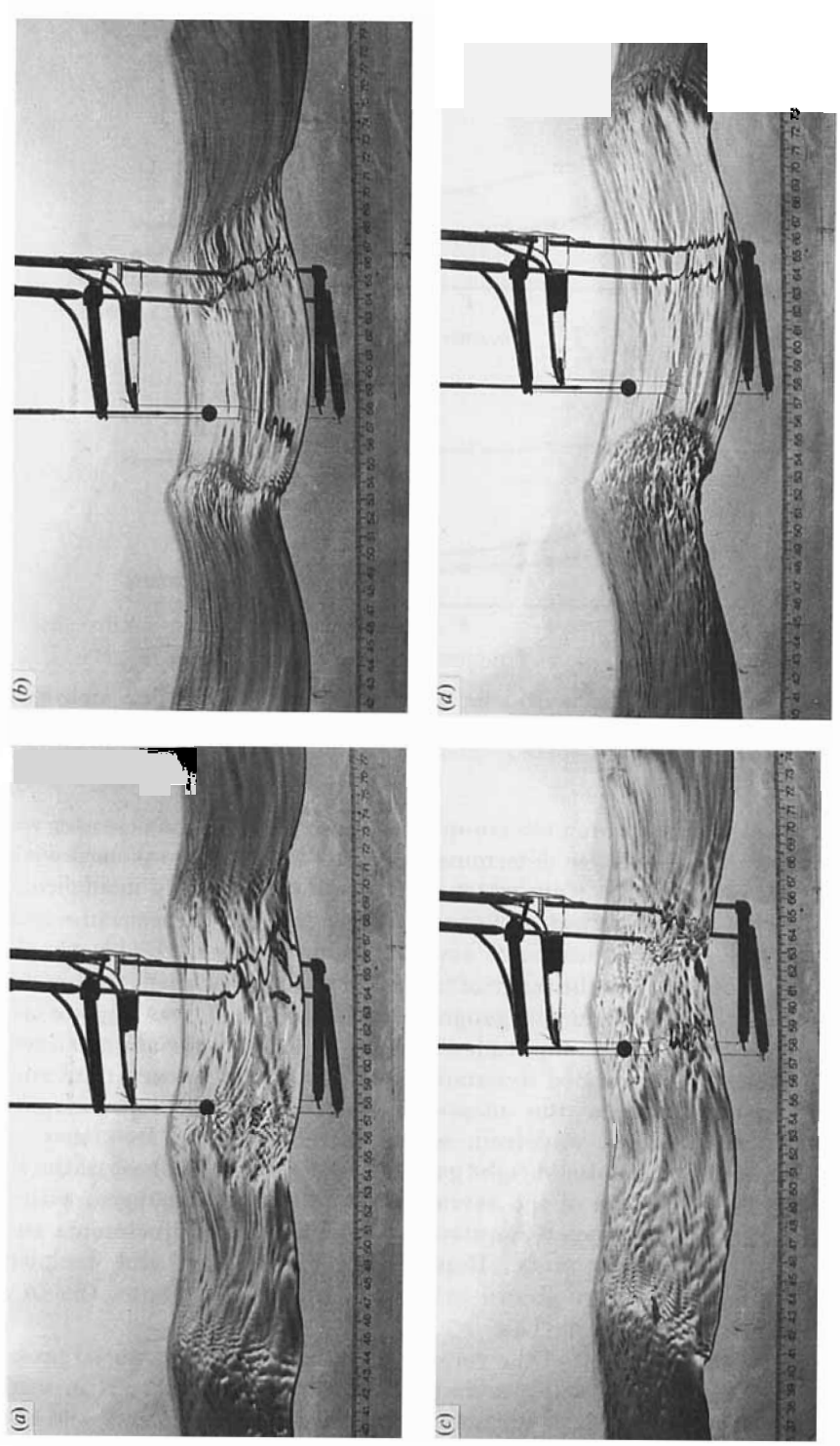

FIGURE 8. Photographs showing typical breaking and incipient breaking waves in the propagating wind-wave experiments. The horizontal lengthscale is in cm. The wind speed was 5.5 m/s from left to right. (*a*) 3.35 Hz incipient breaking waves. (*b*) 3.35 Hz breaking waves. (*c*) 2.85 Hz incipient breaking waves. (*d*) 2.85 Hz breaking waves.

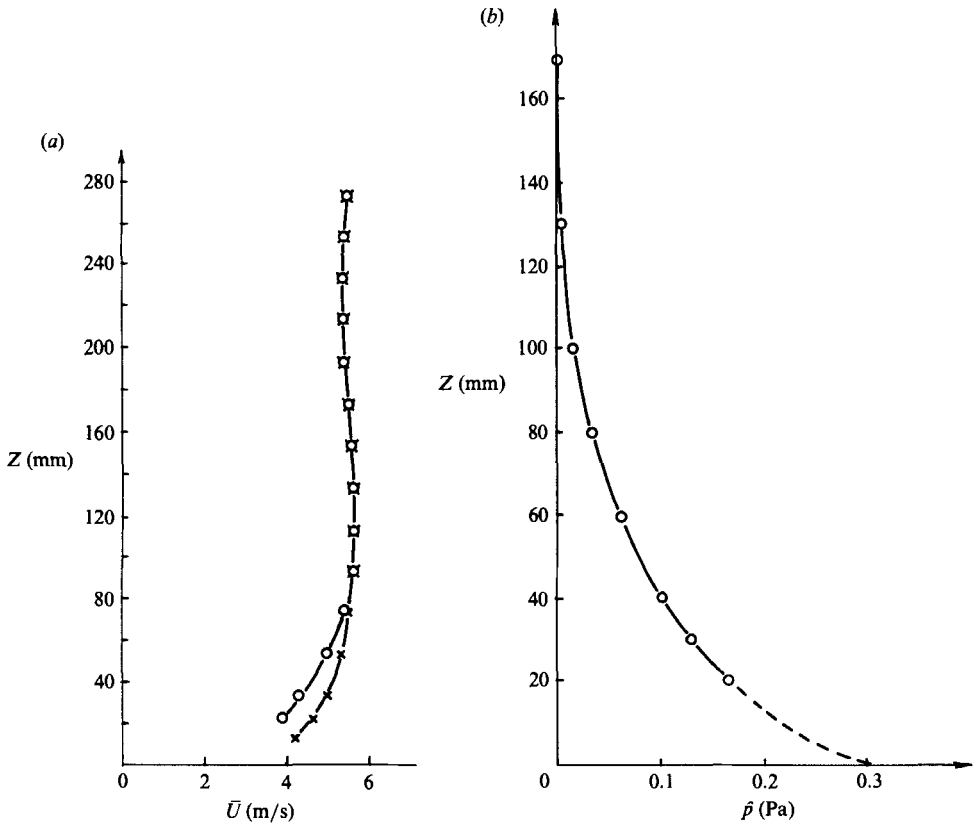

FIGURE 9. (*a*) Vertical profile of the mean velocity in the centre of the working section (open to the atmosphere), for the propagating wind-wave experiments: ×, wind ripples (no mechanically triggered waves); ○, 2.85 Hz mechanically triggered, near continuously breaking waves. (*b*) Vertical profile of the mean wave-induced pressure of the fundamental, for 2.85 Hz breaking waves. Free-stream windspeed = 5.5 m/s.

intercomparisons were made for two different upper boundary conditions at the roof of the wind channel (roof section closed or roof section open over the working section), to verify that such spurious effects did not significantly alter the results. Although the effect on the wave-induced pressure field appeared to be secondary, the main experiments were performed with the roof section open to the atmosphere over a fetch equivalent to several wave lengths, centre on the working section. This 'open roof' experimental configuration required the installation of an axial flow fan at the wind channel inlet to provide an additional blowing mode which was used also for the closed roof experiments to maintain uniformity. It was felt that the 'open roof' condition was more representative of natural conditions, and it was reassuring that the wave-induced pressure now decayed to zero in the free stream. The presence of the open roof section did not adversely effect the vertical uniformity of the mean velocity profile in the free stream. These details are given in figure 9, which shows the vertical profiles of the mean velocity and the wave-induced pressure fields.

The data runs consisted of sets of ensembles of 16 records, with each record of 8 s duration sampled at 32 Hz, representing a total sample size of about 400 waves. The pressure disk and Kiel tube data for both breaking and incipient breaking situations were recorded and processed spectrally, as described in detail in §3.2. The

Kiel (total) tube data was included to assess the contribution of the dynamic velocity term $\frac{1}{2}\rho U^2$ to the pressure disk signal (see equations (2.1), (2.2)).

The total windstress for each of these two wave conditions was determined on the basis of the logarithmic mean velocity profile method using laser anemometry to determine the mean velocity profile. This instrument was chosen on the basis of its linearity in this flow region of intrinsically high turbulence level and vertical gradient of turbulence level, factors which could introduce significant errors in comparable Pitot-static determinations. Typically, temporal averaging over 250 s was required to obtain a stationary local mean velocity estimate.

3. Data analysis

3.1. *Stationary-wave configuration*

The measured pressure and velocity distributions are presented graphically in §4.1. In addition, files of the extrapolated surface pressure and elevation data were created on a VAX 11/750 for further processing as described below. Taut spline fits (De Boor 1978, ch. 16) to the surface elevation and pressure data (shown in the following section) enabled accurate determination of zero crossings of the surface elevation as well as interpolation of local surface slopes for the purpose of calculating accurate values of slope–pressure correlations over different sections of the wavy water surface. To confirm that the numerical interpolation scheme was not introducing any spurious contributions, correlations of $\langle \eta\eta_x \rangle$ were computed between successive positive-going and negative-going zero-crossings using Simpson's rule for the integrations. Ideally, this correlation should vanish identically. The ratio

$$\frac{\langle \rho_a g\eta\eta_x \rangle}{\langle p\eta_x \rangle}$$

represents the ratio of spurious momentum flux introduced by inaccuracies in the profile and zero-crossing detection to the determined momentum flux due to the measure surface pressure. Typically, this ratio was found to be less than $O(10^{-6})$. On this basis it was concluded that computationally reliable estimates of $\langle p\eta_x \rangle$ were obtained, limited only by the accuracy of the data. The results for the pressure–slope correlations obtained for the different wind speeds over different sections of the wave profile are presented in §4.1. The taut spline fits also facilitated an assessment of the conformity of the stationary breaking wave surface elevation profile to the characteristic breaking wind-wave shape parameters described by Koga (1984), together with a detailed comparison of the surface pressure with appropriate numerical solutions cited in §1.

3.2. *Propagating wave configuration*

The data from the pressure system and the two wave gauges was recorded on a microcomputer via an analog-to-digital computer. Sampling of these three signals occurred 1/4000 s apart as a sampling burst. The sampling of such bursts occurred at a rate of 32 Hz for 8 s. Ensembles of 16 data sets were processed in real time using standard Hanning windowing and cross-spectral analysis based on fast Fourier transform methods. In the course of the data analysis, the calibration data and the frequency response characteristics of the instruments, reported in figure 7, were introduced to correct the data. The analysis provided r.m.s. slope and pressure magnitudes and their phase difference as a function of frequency, as well as the wave-

coherent momentum flux, i.e. the integrated covariance between pressure and slope. Similar cross-spectral analysis techniques were also used to verify the performance of the two-probe slope gauge prior to and following each of the data runs and to quantify the dynamic velocity contribution to the disk pressure and to the disk pressure–slope covariance. For the latter, the output from the Kiel tube was correlated with the local slope signal and the average contributions of the dynamic velocity terms $0.112\langle\frac{1}{2}\rho_a U^2\rangle$ and $0.112\langle\frac{1}{2}\rho_a U^2(\partial\eta/\partial x)\rangle$ to the disk determinations of local pressure and form drag respectively were determined. The pressure and form drag data were then corrected by these respective contributions. Typical magnitudes of this correction are discussed in §4.2.

Owing to the 10–15% attenuation of the measured surface pressure due to the fixed sensor height just above the crest level (see figure 5*b*), pressure and form drag were measured at various heights above the mean water level and extrapolated to this level to obtain the surface value. An alternate extrapolation procedure was also implemented in which each sampled pressure value was extrapolated to the surface based on an exp $(-kz)$ dependence, where z is the distance of the local water surface elevation below the fixed probe and k is the dominant wavenumber. This assumed vertical dependence of the wave-induced pressure field was found to be a reasonable approximation in both the stationary and propagating wave studies. As discussed in §4.2, the results were relatively insensitive to the surface extrapolation method used.

The percentage of breaking waves passing through the measurement site, a fundamental parameter in this study, was assessed using a detection scheme based on the slope discontinuity at the toe of the spilling region of breaking wind waves. Here, the wave elevation was sampled at 200 Hz in 60 s bursts and a time series of the effective instantaneous slope was calculated as the product of the first difference of the elevation time series with the phase speed of the dominant waves. The statistics of the slope exceedance were calculated on-line for all the dominant waves passing the measurement site. This determination was repeated several times to reduce the statistical variability, and it was found that this method provided a reliable discrimination between the incipient-breaking and spilling-breaking waves in this study. The results are presented in the following section. Also, an auxiliary analysis of the sampled surface elevation time series for the propagating breaking-wave cases was made using the characteristic wave analysis methodology of Koga (1984), and this confirmed that the shape parameters of the breaking waves in this study conformed closely to those determined by Koga (1984) for actively breaking wind waves.

4. Results

4.1. *Stationary-wave configuration*

The variation of the surface wind pressure along a composite water surface comprising sections of breaking and unbroken waves is reported in figure 10 for the different wind speeds investigated. Also shown is the distribution of the surface pressure–surface slope product or equivalently the local form drag.

Several key features are revealed by these distributions. Downwind of the breaking crest, the surface pressure peak is shifted ahead of the trough by around 60°–70° for each wind speed. These phase shifts are generally larger than those associated with the unbroken wavy profile, both upwind and downwind from the breaking segment. Of these, the former is the steeper with $ak \sim 0.135$ and shows a decreasing trend in the pressure phase shift with increasing wind speed. Negligible

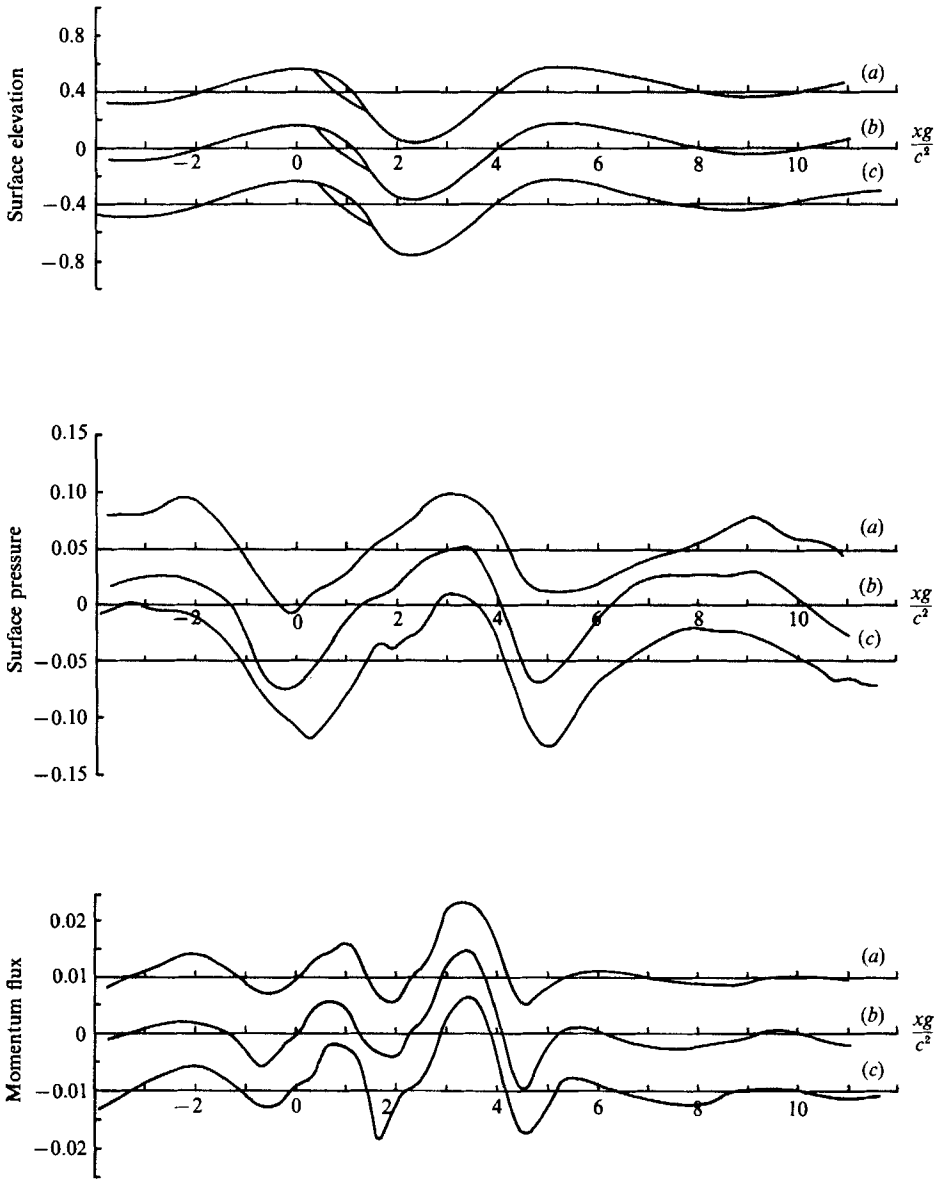

FIGURE 10. Non-dimensional distributions of the mean surface elevation $\eta g/c^2$ (upper curves), mean surface pressure $p/\rho_a U_c^2$ (middle curves) and mean local momentum flux $p\eta_x/\rho_a U_c^2$ (lower curves) for the stationary-wave experiments for different centreline windspeeds (*a*) $U_c/c = 3.29$, (*b*) $U_c/c = 4.81$, (*c*) $U_c/c = 6.84$. The dimensionless horizontal coordinate is xg/c^2 measured downwind from an arbitrary origin at the location of the breaking crest. ($c = 0.79$ m/s; $g = 9.81$ m/s^2; $\rho_a = 1.225$ kg/m^3).

phase shifting is apparent in the unbroken downwind wave trough. It is evident that the larger phase shifts and profile steepness ($ak \sim 0.3$) associated with the breaking-wave section combine to produce the strong downward (positive) momentum flux to the water surface downwind of the breaking-wave trough observed in each realization. The consequences for the wave-coherent momentum flux, i.e. the

wavelength averaged contribution over various subsections of the water surface are reported subsequently in this section.

Figure 11 shows the associated vertical distributions of the mean wind speed and pressure at selected locations along the wave profile, shown for $U_c/c = 3.29$ ($U_\infty/c = 4.29$), and $U_c/c = 6.84$ ($U_\infty/c = 7.84$). The intermediate windspeed case, not shown here, was qualitatively similar. These figures reveal characteristic magnitudes and vertical scales of the wave-induced perturbations over both breaking and unbroken sections of the water surface. The overall vertical extent of the wave-induced motion is consistent with a lengthscale based on the dominant wavelength of the wavetrain, with the pressure effect showing a somewhat larger vertical persistence.

The vertical structure of both the wind velocity and pressure fields shows interesting variation along the wave profile. At the stations upwind of and at the breaking crests, the magnitudes of the wave-induced perturbations to the pressure and velocity fields increase quasi-exponentially as the surface is approached. However, the behaviour in the trough downwind of the breaking crest shows velocities approaching zero and, particularly for the higher windspeed cases, static pressure levels well below those in the trough upwind of the breaking crest. This is a clear manifestation of the separated air flow known to exist in the lee of the breaking crest. From figure 10 it is seen that pressure recovery is delayed until well up the windward face of the downward wave, presumably in association with the reattachment points, as found by Buckles *et al.* (1984) in their study of air flow over steep solid wave forms. Near the crest of this downwind wave, significant flow acceleration results in a strong negative pressure peak, with the influence of the wake created by the separated flow region apparent in the near-surface velocity distribution. The wake flow may still be detected in the downwind unbroken wave trough velocity profile. At this location and the crest downwind of it, the vertical pressure distribution has recovered a characteristic quasi-exponential behaviour.

The computations of average momentum flux $\langle p\eta_x \rangle$ along various wavelength sections of the water-surface profile are shown in non-dimensional form in table 1 for the three windspeed cases investigated. The localization of relatively large concentrations of wave-coherent momentum flux to the breaking-wave segments is immediately apparent. A consideration of the implications of their absolute levels is presented in §5.

An analysis of the breaking-wave shape parameters following Koga (1984) indicated that the stationary breaking-wave profile had a somewhat broadened crest region when compared with propagating breaking-wave profile shapes, as is evident from the realizations shown in figures 2 and 8(*b*), (*d*). As pointed out earlier, this was one of the factors which motivated the propagating-wave experiments.

4.2. *Propagating-wave configuration*

The vertical profiles of the mean velocity and wave-induced pressure in the working section for the results to be described were shown previously in figure 9. Also, prior to presenting the detailed dynamical results, it is appropriate to quantify the wave-breaking statistics which provide a useful measure of the level of breaking activity characteristic of these experiments.

The slope exceedance data for the two wavelengths is shown in figure 12 from which it is evident that the breaking and incipient breaking waves can be distinguished objectively: a slope threshold of 0.50–0.55 provides a clear separation, consistent with visual inspection, of the two classes. Thus for the breaking waves realized here, typically 70% were undergoing spilling breaking as they passed the

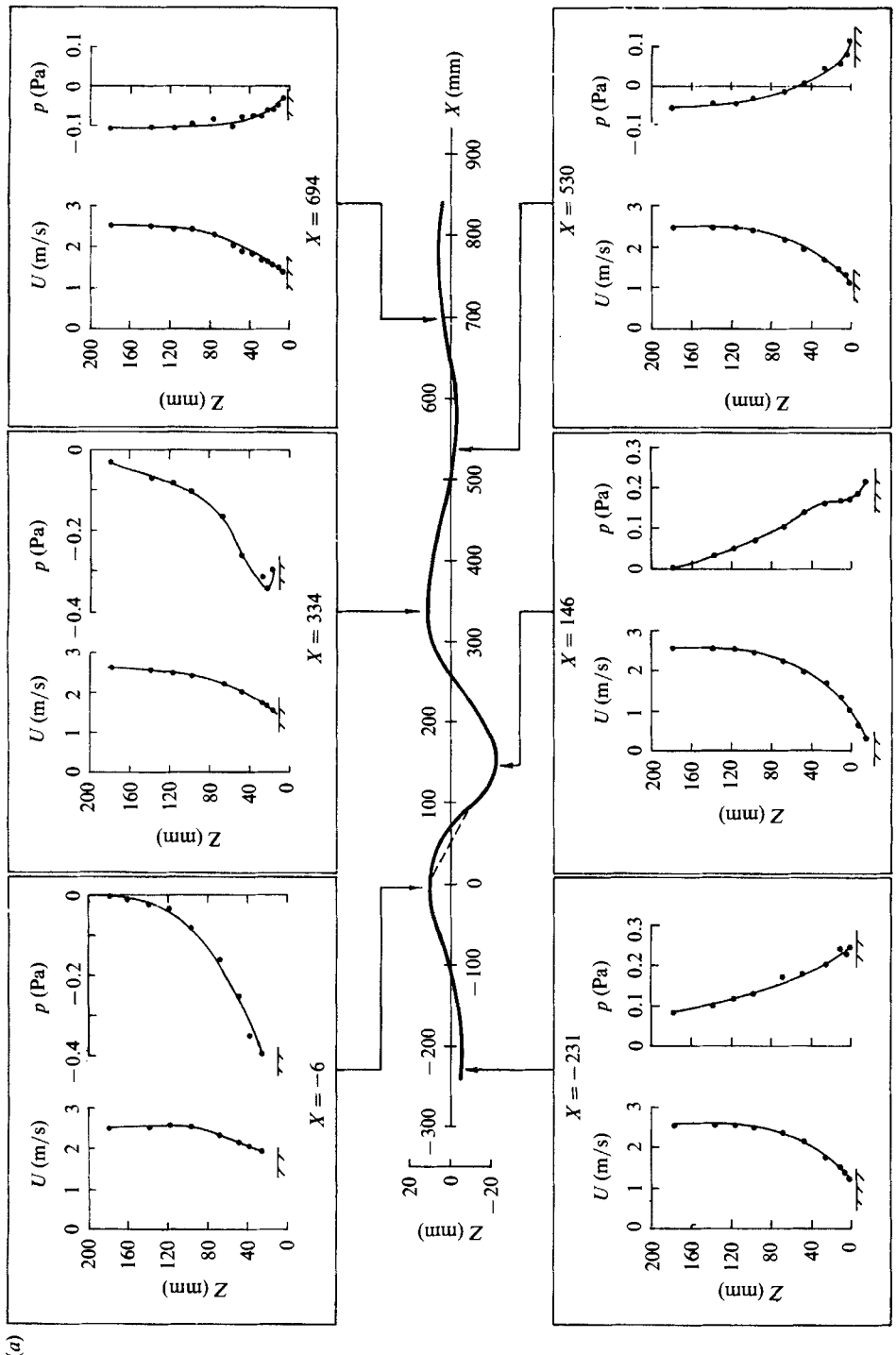

(a)

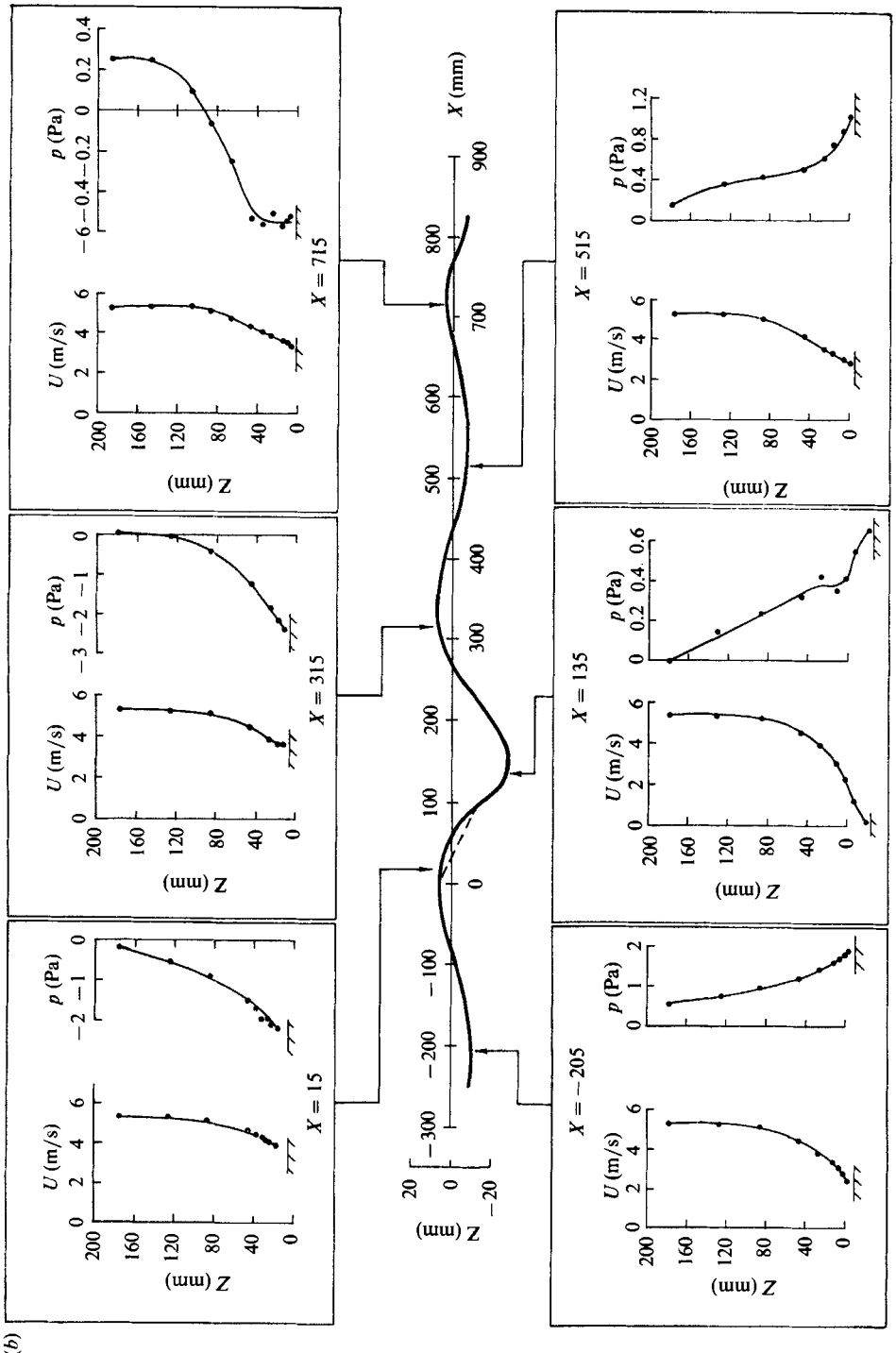

FIGURE 11. Vertical profiles of the mean wind speed U and mean static pressure p at the indicated stations along the stationary wave profile for different centreline wind speeds. (*a*) $U_c = 2.6$ m/s $[U_c/c = 3.29]$, (*b*) $U_c = 5.4$ m/s $[U_c/c = 6.84]$.

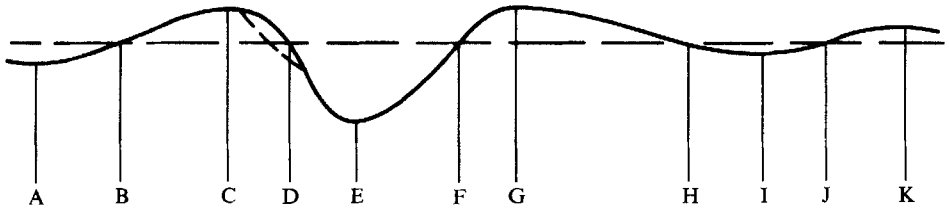

	U_c/c	3.29	4.81	6.84
	AE	0.92	−0.03	1.16
	BF	3.05	2.45	3.82
	CG	3.14	2.35	3.43
Section	DH	2.09	0.80	2.59
	EI	2.21	0.71	2.05
	FJ	0.03	−1.38	−0.61
	GK	−0.03	−0.62	−0.02

TABLE 1. Variation of the wavelength-averaged non-dimensional form drag $10^3 \langle p\eta_x \rangle / \rho_a U_c^2$ against the non-dimensional centreline windspeed U_c/c for the various wavelength sections of the stationary breaking-wave profile shown in the inset. The wind direction is from left to right. $\rho_a = 1.225\ \mathrm{kg/m^3}$, $c = 0.79\ \mathrm{m/s}$.

measurement site, while at most only 1–3% of the incipient breaking waves were detected as breaking.

Detailed profiles of the mean wind velocity over the breaking and incipiently breaking waves are shown in figure 13 in standard linear–logarithmic form for the two wavelengths investigated. A reference condition with no mechanical waves is also shown for comparison. It is immediately evident that for the breaking-wave cases, the logarithmic layer region has a larger mean velocity gradient and a greater displacement from the mean water surface. This implies that the friction velocity and roughness length are both enhanced significantly for the breaking waves when compared with the incipient breaking cases. Quantitatively, the friction velocity changed from about 0.37 m/s for the latter to about 0.51 m/s for the breaking waves, for each of the wavelengths investigated. This represents a near-doubling of the windstress from about 1.6 Pa to 3.0 Pa. The roughness length increased from about 0.35 mm to 1.5 mm for the breaking cases. These results highlight the strong local effects associated with the breaking waves on the mean wind profile parameters.

Next we present the pressure–slope covariance and total windstress result with the aim of determining what fraction of the augmentation in the total windstress which accompanies the onset of breaking is due to enhanced form drag. The results of the integrated spectral slope–pressure covariance data at different heights above the mean water level for the various cases are shown in figure 14. In accordance with (2.1), the complementary Kiel tube data provided a correction to the disk-sensed pressure due to the dynamic velocity influence, which amounted to an increase of $O(10\%)$ in p_d to obtain p_s. The projected surface values are indicated, based on extrapolating the vertical profile data to the mean water level and these are in very close agreement with values obtained assuming an exponential decay in the on-line

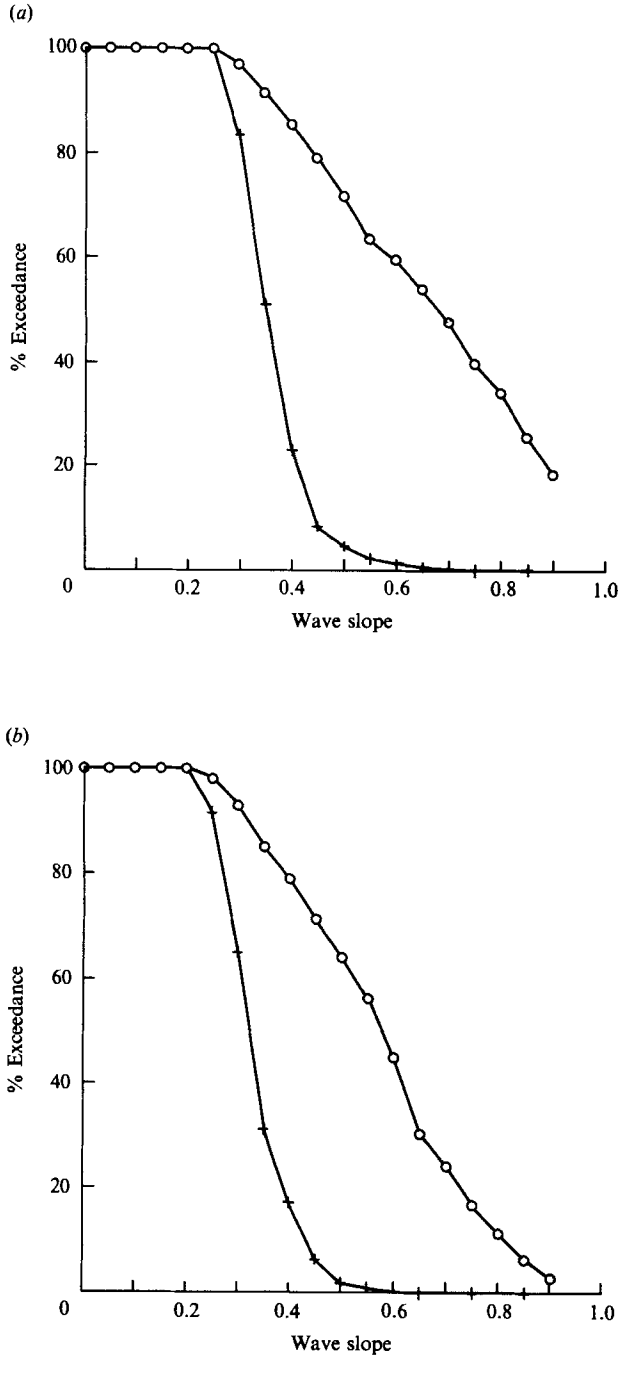

FIGURE 12. Slope exceedance statistics for the propagating wind-wave experiments: ○, breaking waves; +, incipient breaking waves. (*a*) Peak frequency = 2.85 Hz. (*b*) Peak frequency = 3.35 Hz. Free-stream windspeed = 5.5 m/s.

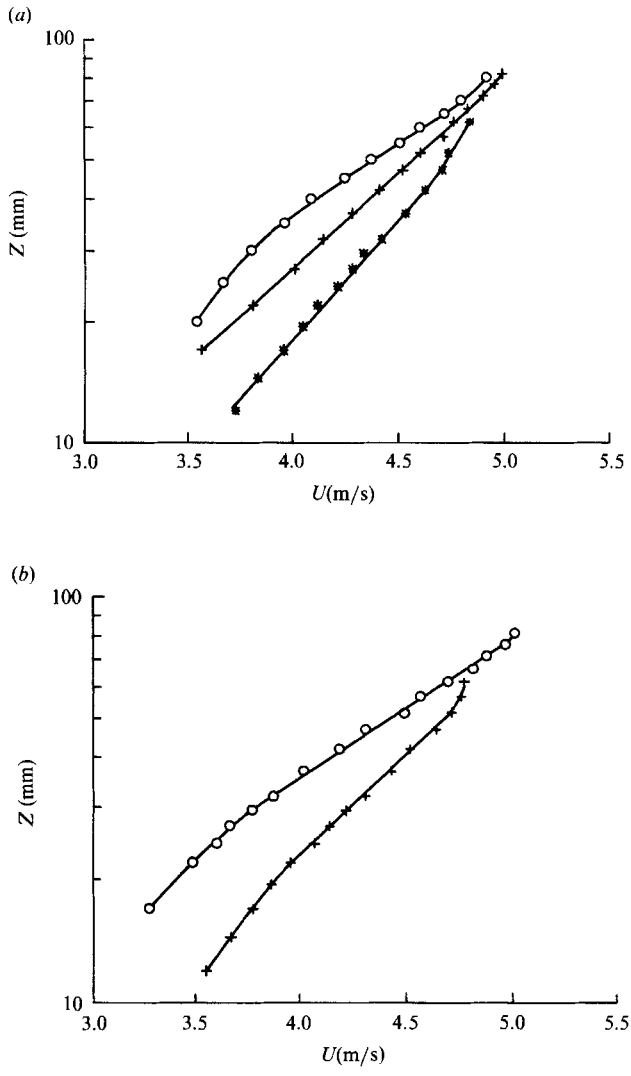

FIGURE 13. Mean wind velocity profiles in the near-surface layer embracing the logarithmic profile region for the propagating wind-wave experiments: ○, breaking waves; +, incipient breaking waves. (*a*) Peak frequency = 2.85 Hz. (*b*) Peak frequency = 3.35 Hz. Also, ✱, the case of wind ripples only (no mechanically triggered waves) is shown in (*a*). Free-stream windspeed = 5.5 m/s.

analysis, as described earlier in §3.2. These results are summarized in table 2, together with the associated wave and total stress data. It is immediately evident that most of the total stress enhancement associated with breaking is reflected in the correspondingly large increase in the form drag.

The implications of these results are discussed in the following section.

5. Discussion

The detailed stationary-wave profile measurements of surface pressure distribution (figure 10), vertical profiles of mean velocity and pressure (figure 11) and the derived results in table 1 serves to highlight important local differences in the wind flow over

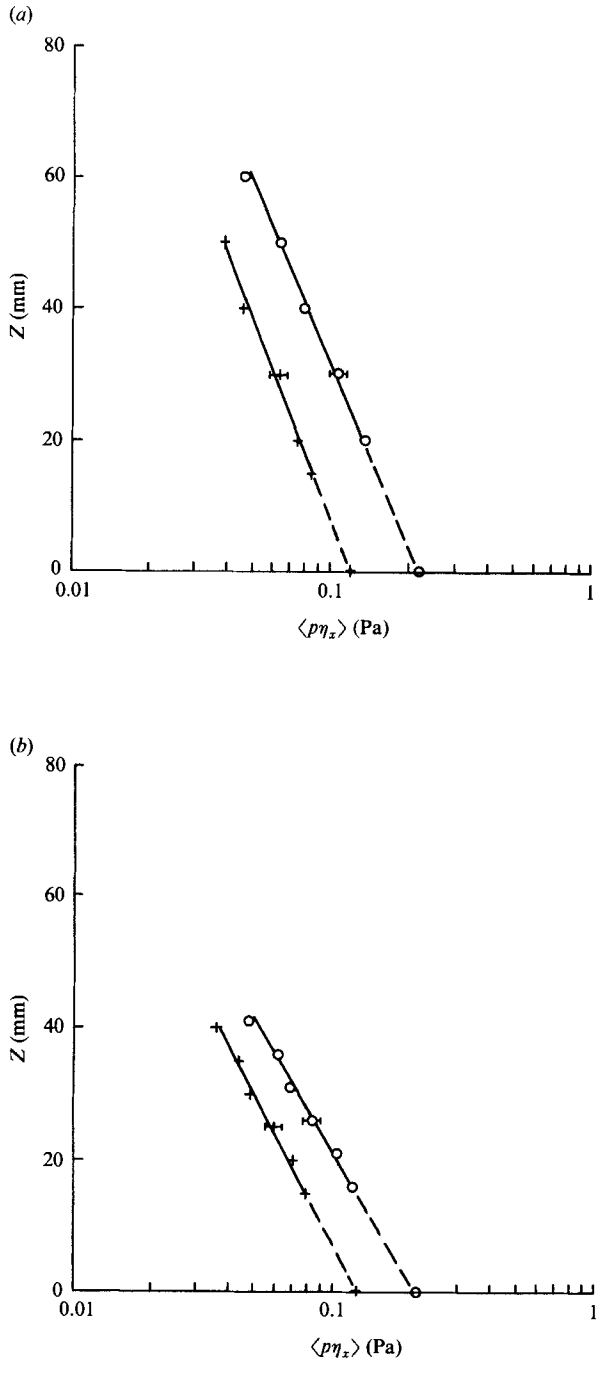

FIGURE 14. Vertical profiles of the form drag $\langle p\eta_x \rangle$ for the propagating wind-wave experiments. (*a*) Peak frequency = 2.85 Hz. (*b*) Peak frequency = 3.35 Hz. ○, breaking waves; +, incipient breaking waves. Free-stream windspeed = 5.5 m/s.

Mechanical wave frequency (Hz)	Wave condition	r.m.s. wave slope	Non-dimensional friction velocity $10^2 u_*/U_\infty$	Roughness length z_0 (mm)	Non-dimensional form drag $10^3 \tau_w/\rho_a U_\infty^2$	Non-dimensional windstress $10^3 \tau/\rho_a U_\infty^2$	Phase angle of fundamental (slope leads pressure. deg)
0	wind ripples at 2.5 m fetch	N/A	5.36	0.078	N/A	2.81	N/A
2.85	incipient breaking	0.25	6.93	0.33	3.56	4.70	75
2.85	near-continuous breaking	0.28	8.96	1.41	6.48	7.88	57
3.35	incipient breaking	0.25	6.62	0.37	3.72	4.29	70
3.35	near-continuous breaking	0.27	9.29	1.61	6.34	8.45	59

TABLE 2. Summary of form drag and windstress results for the propagating wave experiments. Free-stream windspeed $U_\infty = 5.5$ m/s.

the breaking and unbroken sections of the wave profile, and to quantify their implications for wind-wave interactions. In figure 11, the presence of air flow separation in the trough downwind of the breaking crest is evident from the near-zero mean velocity and poor static pressure recovery, which has important consequences for the surface pressure distribution and therefore the form drag. Reference to figure 10 shows that while the pressure minima occur over the crests, the pressure maximum downwind of the breaking crest is shifted out of the trough, up the windward face of the wave ahead. Typically, for the realizations studied here, phase shifts relative to the trough of the order of 60°–70° were observed. In comparison, much smaller phase shifts were found in the neighbouring upwind and downwind unbroken trough regions, but for these adjacent unbroken sections of the wave profile, the local steepness was much lower. Reference to the numerical model calculations cited in §1 (e.g. Gent & Taylor 1976; Gent 1977; Taylor *et al.* 1977) for unbroken (Stokes) wave profiles shows that the phase shift of the pressure maximum relative to the trough increases with wave steepness, with predicted levels for strong forcing ($u_*/c \sim 0.67$) of about 30° for moderate waveslope (0.157), increasing to about 60° for a slope of 0.314. Despite the differences in the wave profile geometry and surface boundary conditions for the numerical model and the present stationary breaking-wave realization, the numerical model predictions suggest the possibility that the enhanced phase shift associated with the breaking wave may simply reflect the increased local wave profile steepness, irrespective of whether the wave is breaking or not. This is one basic issue which is not resolved by the present stationary-wave configuration: another is whether the amplitude of the pressure perturbation associated with such a spatially inhomogeneous wave profile slope is representative, and indeed, whether the breaking-wave results are influenced significantly by the details of the shape of the breaking-wave profile, here created predominantly by hydrodynamic forcing by a subsurface obstacle, rather than by excess wind forcing. These basic issues could not be resolved by using the stationary-wave profile configuration, as efforts to set up a very steep unbroken wave were unsuccessful: the two-dimensional character of obstacle-induced unbroken waves was found to deteriorate sharply for slopes above about 0.1.

With the aim of elucidating the basic issues unresolved by the stationary-wave results, the propagating-wave measurements described in §2.2 were designed to separate the usually concomitant effects of wave breaking and large wave steepness. The cross-spectral analysis results reported in §4.2 and summarized in table 2 demonstrate clearly that there is a significant phase shift in the pressure field (typically 15°–20° for the fundamental), with appreciable form drag for very steep unbroken waves. However, following the onset of breaking, there are large increments, typically 100%, in the pressure phase shift, in the form drag and in the windstress, which are additional to the corresponding levels for comparably steep unbroken waves. These results therefore highlight the dominant influence of form drag of steep waves in the windstress, as has been noted by previous authors, and also demonstrate unambiguously the very significant increase in the form drag and consequent windstress augmentation contributed during active wave breaking.

It is useful to relate the propagating wave findings to the stationary-wave results and to previous measurements and numerical model results. The cross-spectral analysis results for the propagating breaking-wave cases (table 2) show there was a typical pressure phase shift of around 30° for the fundamental, whereas Wu *et al.* (1977) reported about 40°–45°. However, Wu *et al.* (1977) do not appear to have taken into account the phase lag of their wave gauge. If the typical phase lags for the

wave height gauges used in this study are applicable, then phase lag corrections of 12°–15° would be appropriate, which would reconcile most of the discrepancy in the phase. Also, a comparison of the pressure amplitude level reported by Wu *et al.* (1977) indicates a close correspondence with the present propagating-wave levels for both breaking and incipient breaking waves, with the non-dimensional wave-coherent pressure amplitude $\hat{p}/\rho_a U_\infty^2 \sim 0.01$. This is also in close correspondence with the surface pressure amplitude predicted by Gent & Taylor (1977) for comparable wind forcing and wave slope conditions. In comparison the stationary breaking-wave pressure amplitude is somewhat lower, which is attributed to the very reduced wave profile slope immediately upwind and downwind of the breaking-wave section. This indicates the likely effects of large spatial inhomogeneity in the steepness of the wave profile, here stronger than might occur during typical wind-wave modulation. However, further pursuit of this aspect is beyond the scope of the present investigation. Also, as was described in §1, on the basis of viscous sublayer measurements in the water, Okuda *et al.* (1977) claimed that skin friction effects dominated form drag effects for highly forced wind waves at very short fetches. This is not in accord with the present finding that the form drag was dominant, based on a more direct determination, nor with the results of Buckles *et al.* (1984) over very steep solid waves, for which the skin friction was found to be about one-ninth of the form drag. However, as simultaneous form drag and shear stress measurements were not made here or by Okuda *et al.* (1977), a reconciliation must await a future study.

The wave-induced distortions to the wind surface pressure field described above have important implications for the processes of momentum and energy flux to the wave field. Although the following discussion focuses on momentum flux, a parallel discussion is appropriate for energy flux.

It is of interest to examine related basic aspects of the present propagating wave results in relation to previous wind-wave tank results. The wind friction velocity u_* has been used extensively as a key parameter in quantifying wind-wave interaction processes. According to detailed laboratory studies (e.g. Plant & Wright 1977), over a wide range of fetches in their wind-wave tanks,

$$u_* \sim 0.022(\pm 10\%)\, U_\infty^{1.5}, \tag{5.1}$$

where U_∞ is the reference free-stream windspeed in m/s. For such wave-tank situations, the resultant u_* arises from the integrated effects of the wind flow over a strongly amplitude-modulated wave field with intermittently breaking dominant waves, whose modulational and breaking statistics have not been monitored. In relation to the representative u_* level expressed by (5.1), the propagating wind-wave results found here under controlled breaking or incipient breaking conditions point out the strong influence of the degree (or intermittency) of wave breaking on the resultant u_*. For wind ripples only, the observed value of $u_* = 0.295$ m/s for a reference windspeed of 5.5 m/s is in close agreement with (5.1). However for controlled incipient breaking-wave conditions, u_* increased by about 40% above the representative level and for the almost (70%) continuously breaking waves, u_* rose by about 90% above the representative level. These results together with the concomitant form drag levels shown in table 2 demonstrate convincingly the dominant role of the form drag in the momentum flux to the wind-wave field and in the overall windstress. These results also highlight the potential importance of wave breaking in further augmenting these basic quantities.

It is also appropriate to enquire how the observed u_* level, as parameterized by (5.1), results from the various contributions: skin friction and form drag due to

unbroken and breaking waves. A detailed quantitative resolution of this fundamental question is beyond our present knowledge. However, as pointed out above, u_* represents an average over the strongly amplitude modulated, intermittently breaking wind-wave field. For proposed wind-induced growth rate formulae, such as Plant (1982) (see equation (5.2)), the wave-coherent momentum flux τ_w, assumed to be predominantly form drag, has been shown (Plant 1982) to be proportional to the upwind/downwind mean squared slope and that for typical mean wind-wave slopes, τ_w provides a dominant contribution to the windstress. With such a strong dependence on the local dominant wave slope, the observed representative mean windstress or u_* might be expected to reflect the integrated effects of reduced levels near the amplitude envelope minima, elevated levels near the envelope maxima, with additional intermittent increments arising from the transient breaking events. However, the absence of quantitative knowledge of the relevant statistics of the wind-wave field precludes a more detailed analysis.

It remains to attempt to relate the present findings to the spectral wind input source function [S_{in}] and also to reported wind-wave growth rate parameterizations, such as Plant (1982), who proposed that the dimensionless growth rate β^* ($= \beta/\omega$) was given empirically by

$$\beta^* = 0.04(\pm 0.02)(u_*/c)^2 \quad \text{for } u_*/c > 0.1, \tag{5.2}$$

where u_* is the representative mean wind friction velocity, deduced from the mean velocity profile slope in the logarithmic layer, or from an average of the fluctuating wind shear stress. A $\cos\theta$ angular dependence is usually assumed in (5.2), where θ is the angle between the direction of the wind and wave component, but this has been suppressed here as all the present data is for co-directional wind and waves.

It should be noted that S_{in} represents only the input from the atmosphere while the actual growth rate of a given spectral component is the resultant of wind input as well as nonlinear spectral transfers and dissipation. If the growth rates are based only on wind input measurements (such as Synder *et al.* 1981) then these growth rates are equivalent to S_{in}. In Plant (1982), both wind input measurements and observed spectral rates of wave growth were used in determining (5.2) but Plant pointed out that the latter were chosen from situations where wind input was the dominant source for wave growth. Such situations include monochromatic wave growth and initial transient growth of very short wave components. Hence (5.2) may be regarded as equivalent to the input source function. Using the representative u_* (as expressed by (5.1)) as reference, the present results provide a basis for parameterizing the input source function, or the equivalent effective growth rate, for wind flow over breaking waves. If, as the data indicates, the form drag dominates the windstress over breaking waves, then the effective dimensionless growth rate β_b^* for breaking wind waves is given by

$$\beta_b^* = (1/\omega M)\,\mathrm{d}M/\mathrm{d}t, \tag{5.3}$$

where $\mathrm{d}M/\mathrm{d}t$ is the measured momentum flux $\langle p\,\partial\eta/\partial x\rangle$ to the breaking waves, available for the case studied in table 2 and ω is the intrinsic frequency. M is the momentum density of the breaking waves and needs to include some estimate for the momentum of the spilling zone fluid. Thus

$$M \sim \tfrac{1}{2}\rho_w \omega a^2 + \rho_w c A_b/\lambda_b, \tag{5.4}$$

where a is the breaking-wave amplitude, c is its phase speed, λ_b is its wavelength and A_b is the average cross-sectional area of the spilling zone. An analysis of breaking-

wave profiles recorded at high sample rates during the breaking-wave statistics measurements allows an assessment of spilling zone geometries for transients, spilling breaking wind waves. Based on this analysis, it was found that an average value for $A_b/\lambda_b^2 \sim 0.002$ appears representative. Thus for the cases reported in table 2, and using the reference u_* for a given windspeed as given by (5.1),

$$\beta_b^* = 1/\omega M \, \mathrm{d}M/\mathrm{d}t \sim 2\rho_a u_*^2/\rho_w[\tfrac{1}{2}\omega^2 a^2 + 0.002\,\omega c \lambda_b].$$

Using $\omega = kc$ and assuming $ak \sim 0.3$ at breaking,

$$\beta_b^* \sim 0.04(u_*/c)^2, \tag{5.5}$$

which is in close correspondence with the Plant (1982) relation (5.2) proposed for arbitrary wave slope.

A similar analysis for the incipient breaking-wave results shown in table 2 provides a measure of the effective growth rate for very steep waves, just prior to breaking. It may be seen from this table that the form drag magnitude is about $1.4\,\rho_a u_*^2$ (based on the reference u_* given by (5.1)) and this represents about 83% of the measured windstress. Under the assumption that $\tau_w = 1.4\,\rho_a u_*^2$, the effective dimensionless growth rate for incipient breaking waves β_i^* is then

$$\beta_i^* = \frac{1.4\rho_a u_*^2}{0.5\rho_w \omega^2 a^2}.$$

With $\omega = kc$ and assuming $ak \sim 0.3$ at incipient breaking

$$\beta_i^* \sim 0.04(u_*/c)^2, \tag{5.6}$$

again in close correspondence with (5.2).

In the context of including wave-breaking effects in the parameterization of the wind input source function S_{in} for numerical wind-wave spectral evolution calculations, some care is needed in applying the present findings. These results show that for a given windspeed, increased levels of windstress and waveform drag are associated with the occurrence of breaking waves, for which, however, the statistics are largely unknown. Also, it was found that when expressed relative to the momentum density for breaking waves (which includes the momentum of the spilling region), the effective growth rate conforms closely to Plant's correlation (5.2). Despite this apparent convenience, it should be noted that the usual spectral formulations of S_{in} are based on wind input growth rates together with the waveheight spectral density, which does not include contributions from spilling regions of breaking waves. Thus, embodying the effects of breaking waves in S_{in} constitutes a considerable challenge.

The effective input growth rate (5.2) implies that the momentum added to the wave field per wave period T expressed as a fraction of the wave momentum is given by $2\pi\beta$, where $\beta = \omega\beta^*$ is the dimensional growth rate arising from (5.2), (5.5) or (5.6). From this result, for the 'strongly forced' ($u_*/c \sim 1$), near-continuously breaking propagating waves in this study, the momentum flux from the wind added each wave period represents about 25% of the wave momentum. This indeed represents strong wind forcing. For the system of breaking waves to be maintained in this quasi-stationary state, this excess momentum flux must be transferred to the underlying surface current at the same rate. We note that similar considerations for fetch-limited growth of wind waves have been discussed by Mitsuyasu (1985). For such developing wind-wave fields, he estimates that almost all ($O(95\%)$) of the momentum flux to the wind-wave field is transferred to surface currents, with only a small

proportion ($O(5\%)$) being advected away by the wave field. Also, the present findings on the strong influence of steep waves on u_* directly support the viewpoint that the parameterization of the drag coefficient

$$C_z = \frac{u_*^2}{U^2(z)},$$

where $U(z)$ is the mean windspeed at height z, should depend on the sea state, as has been suggested by many authors (e.g. Geernaert, Katsaros & Richter 1986).

Finally, the present results have a potentially important impact in the context of scatterometer remote sensing of the windstress using backscattered microwave power returns from very short wind waves. In the field, close-range visual observation indicates that these wave components are often characterized by micro-scale breaking, even under moderate windspeeds. In view of the enhanced backscattered microwave power levels from breaking waves reported by several authors (e.g. Kwoh & Lake 1984; Banner & Fooks 1985), Donelan & Pierson (1987) have made an initial effort to include explicit contributions to the backscattered cross-section from breaking waves to improve the internal consistency, accuracy and reliability of the present interpretive scatterometer algorithms. However, the present study indicates the need to consider more closely the relationship between the incremental effect of wave breaking on the windstress and on the microwave backscattered power in order to account more reliably for this potentially important contribution. Complementary microwave backscatter studies are in progress in the present facility to investigate this aspect and initial results indicate that the effects of the breaking waves on the backscattered power are strongly dependent on the microwave antenna look direction (upwind, downwind, etc.) and the degree to which the microwavelength matches the predominant lengthscales of disturbances in the spilling zones of the breaking waves, as were reported by Banner & Fooks (1985). A detailed account will be published elsewhere on completion of this study.

6. Conclusions

The results of this investigation elucidate a basic physical mechanism for momentum flux from the wind to the wave field which is operative during active wave breaking. It has its basis in the streamline distortion induced by the local air flow separation over breaking waves, which results in significant additional phase shifting of the aerodynamic surface pressure with respect to the wave slope, nearly doubling the pressure phase shift associated with comparably steep incipient breaking waves for the strongly forced cases examined here. This mechanism was found to be responsible for large (typically $O(100\%)$) increments in the form drag in comparison with the form drag measured for incipient breaking waves, and for the correspondingly large enhancement in the windstress following breaking, associated primarily with increased form drag. Even for steep unbroken waves, the results show that under strong wind forcing, the form drag dominates the windstress, confirming the need to include the sea state in the drag coefficient parameterization.

The present findings quantify the strong influence of breaking on the momentum flux to the waves and on the windstress. Although these findings would be expected to apply to all wind-wave scales, it is the very short centimetric wave scales which are likely to be most frequently involved in breaking, on account of their higher growth rates. In the context of satellite remotely sensed windstress determinations

using scatterometry, the present findings indicate the need for further studies of the augmented windstress and microwave backscatter from breaking wind waves.

This contribution forms part of an ongoing programme aimed at investigating fundamental aspects of breaking surface waves at the air–sea interface. The support for this project provided by the Australian Research Grants Scheme is gratefully acknowledged, as is the technical assistance of M. Willoughby during the stationary-wave experiments. The author also gratefully acknowledges the hospitality at the UNSW Water Research Laboratory, where this investigation was carried out.

REFERENCES

AL-ZANAIDI, M. A. & HUI, W. H. 1984 Turbulent airflow over water waves – a numerical study. *J. Fluid Mech.* **148**, 225–246.

BANNER, M. L. 1986 A comparison of the wave-induced momentum flux to breaking and non-breaking waves. In *Wave Dynamics and Radio Probing of the Sea Surface* (ed. O. M. Phillips & K. Hasselmann), pp. 321–333. Plenum.

BANNER, M. L. 1988 On the mechanics of spilling zones of quasi-steady breaking waves. In *Sea Surface Sound* (ed. B. R. Kerman), NATO ASI series C: Math. and Phys. Sciences vol. 238, pp. 63–70. Dordrecht: Kluwer.

BANNER, M. L. & FOOKS, E. H. 1985 On the microwave reflectivity of small-scale breaking water waves. *Proc. R. Soc. Lond.* A **399**, 93–109.

BANNER, M. L. & MELVILLE, W. K. 1976 On the separation of air flow above water waves. *J. Fluid Mech.* **77**, 825–842.

BARNETT, T. P. & KENYON, K. E. 1975 Recent advances in the study of wind waves. *Rep. Prog. Phys.* **38**, 667–729.

BUCKLES, J., HANRATTY, T. J. & ADRIAN, R. J. 1984 Turbulent flow over large amplitude wavy surfaces. *J. Fluid Mech.* **140**, 27–44.

CHANG, P., PLATE, E. J. & HIDY, G. M. 1971 Turbulent air flow over the dominant component of wind-generated water waves. *J. Fluid Mech.* **47**, 183–208.

CSANADY, G. T. 1985 Air–sea momentum transfer by means of short-crested wavelets. *J. Phys. Oceanogr.* **15**, 1486–1501.

DE BOOR, C. 1978 *A Practical Guide to Splines*, Springer. 392 pp.

DONELAN, M. A. & PIERSON, W. J. 1987 Radar scattering and equilibrium ranges in wind-generated waves with application to scatterometry. *J. Geophys. Res.* **92**, 4971–5029.

GEERNAERT, G. L., KATSAROS, K. B. & RICHTER, K. 1986 Variation of the drag coefficient and its dependence on sea state. *J. Geophys. Res.* **91**, 7667–7679.

GENT, P. R. 1977 A numerical study of air flow above water waves. Part 2. *J. Fluid Mech.* **82**, 349–369.

GENT, P. R. & TAYLOR, P. A. 1976 A numerical model of the air flow above water waves. Part 1. *J. Fluid Mech.* **77**, 105–128.

GENT, P. R. & TAYLOR, P. A. 1977 A note on 'separation' over short wind waves. *Boundary-Layer Met.* **11**, 65–87.

KAWAI, S. 1981 Visualization of air flow separation over wind wave crests under moderate wind. *Boundary-Layer Met.* **21**, 91–104.

KAWAI, S. 1982 Structure of air flow separation over wind wave crests. *Boundary-Layer Met.* **23**, 503–521.

KOGA, M. 1984 Characteristics of a breaking wind-wave field in the light of the individual wind-wave concept. *J. Ocean Soc. Japan* **40**, 105–114.

KWOH, D. S. W. & LAKE, B. M. 1984 A deterministic, coherent, and dual-polarized laboratory study of microwave backscattering from water waves. Part I. Short gravity waves without wind. *IEEE, J. Oceanic Engng* OE-9, **5**, 291–308.

MITSUYASU, H. 1985 A note on the momentum transfer from wind to waves. *J. Geophys. Res.* **90**, 3343–3345.

MITSUYASU, H. & HONDA, T. 1982 Wind-induced growth of water waves. *J. Fluid Mech.* **123**, 425–442.

MITSUYASU, H. & KUSABA, T. 1988 On the relation between the growth rate of water waves and the wind speed. *J. Ocean Soc. Japan* **44**, 136–142.

LONGUET-HIGGINS, M. S. & SMITH, N. D. 1983 Measurements of breaking waves by a surface meter. *J. Geophys. Res.* **88**, 9823–9831.

OKUDA, K. 1981 Internal flow structure of short wind waves. Part 1. On the internal vorticity structure. *J. Ocean Soc. Japan* **38**, 28–42.

OKUDA, K. 1982*a* Internal flow structure of short wind waves. Part 2. The streamline pattern. *J. Ocean Soc. Japan* **38**, 313–322.

OKUDA, K. 1982*b* Internal flow structure of short wind waves. Part 3. Pressure distributions. *J. Ocean Soc. Japan* **38**, 331–338.

OKUDA, K., KAWAI, S. & TOBA, Y. 1977 Measurements of skin friction distribution along the surface of wind waves. J. Ocean Soc. Japan **33**, 190–198.

PAPADIMITRAKIS, Y. A. 1982 Velocity and pressure measurements in the turbulent boundary layer above mechanically generated water waves. PhD dissertation, Dept. Civil Engng, Stanford University. 445 pp.

PHILLIPS, O. M. 1977 The sea surface, ch. 12 in *Modelling and Prediction of the Upper Layers of the Ocean*. (ed. E. B. Kraus). Pergamon. 325 pp.

PLANT, W. J. 1980 On the steady-state energy balance of short gravity wave systems. *J. Phys. Oceanog.* **10**, 1340–1352.

PLANT, W. J. 1982 A relationship between wind stress and wave slope. *J. Geophys. Res.* **87**, 1961–1967.

PLANT, W. J. & WRIGHT, J. W. 1977 Growth and equilibrium of short gravity waves in a wind-wave tank. *J. Fluid Mech.* **82**, 767–793.

SNYDER, R. L., DOBSON, F. W., ELLIOTT, J. A. & LONG, R. G. 1981 Array measurements of atmospheric pressure fluctuations above surface gravity waves. *J. Fluid Mech.* **102**, 1–59.

WU, H.-Y., HSU, E. Y. & STREET, R. L. 1977 The energy transfer due to air-input, non-linear wave–wave interaction and white-cap dissipation associated with wind-generated waves. *Civ. Engng Tech. Rep.* 207, Stanford University. 158 pp.

YOUNG, I. R. 1983 The response of waves to an opposing wind. PhD thesis, Dept of Civil and Systems Engng, James Cook University, Australia. 289 pp.

XU, D., HWANG, P. A. & WU, J. 1986 Breaking of wind-generated waves. *J. Phys. Oceanog.* **16**, 2172–2178.